Influence of the fluid–fluid drag on the pressure drop in simulations of two-phase flows through porous flow cells

Maxime Cochennec, Hossein Davarzani, Stéfan Colombano, Ioannis Ignatiadis, Michel Quintard, Yohan Davit

Numerical simulations of two-phase flows in highly permeable porous media: Effect of permeability on the drag forces at fluid-fluid and fluid-solid interfaces

Maxime Cochennec

Agence de la transition écologique (ADEME), Angers, France

French Geological Survey (BRGM), Orléans, France

Institut de Mécanique des Fluides de Toulouse (IMFT), Université de Toulouse, CNRS, France

Hossein Davarzani, Stéfan Colombano, Ioannis Ignatiadis

French Geological Survey (BRGM), Orléans, France

Yohan Davit*, Michel Quintard

Institut de Mécanique des Fluides de Toulouse (IMFT), Université de Toulouse, CNRS, France

Abstract

To macroscopically describe two-phase flows in porous media we need accurate modeling of the drag forces between the two fluids and the solid phase. In low-permeability porous media, where capillarity is often dominant, the fluid-fluid drag force is treated similarly to the drag between fluids and solid in the momentum transport equation. Two-phase flows in highly permeable porous media, however, are often characterized by a larger interface area between the two fluids and by thin films developing. In such cases, the fluid-fluid drag is not necessarily negligible and may play an important role in

*Corresponding author

Email address: yohan.davit@imft.fr (Yohan Davit)

the momentum transport equations. Here, we use computational methods to study immiscible cocurrent two-phase flows in a microfluidic device made of an array of cylinders squeezed between two plates in a Hele-Shaw cell. The key idea is to solve 2D Stokes-Darcy equations integrated over the height of the cell, allowing us to explore different permeability ranges by changing the gap between the plates while keeping the 2D geometry in the cell plane unchanged. We use this approach to ask whether the fluid-fluid drag forces affect the pressure drop and how the flow confinement and the capillary number affect the relative importance of the drag forces. We find different behaviors depending on the gap thickness but, in all cases, the fluid-fluid drag plays a significant role in the pressure drop across the cell.
Keywords: Porous media, Hele-Shaw, Drag forces, Pressure drop

1. Introduction

An accurate description of two-phase flows in high-permeability porous media is of major importance for several practical applications. This includes soil remediation in sandy or gravely soils (Fetter et al., 2017), nuclear safety (Clavier et al., 2017), and catalytic fixed-bed reactors (de Santos et al., 1991). However, most of the literature on two-phase flows in porous media focuses on low-permeability porous media in the limit of creeping flows, where surface tension forces often dominate and the capillary, Bond, and Weber numbers are low. In that case, the fluid distribution is well described as two independent flow paths for each phase (Dullien, 1992). The two fluids are predominantly segregated with the non-wetting fluid flowing into the large pores and the wetting fluid flowing through the smallest pores. One con-

sequence is that the area of the fluid-fluid interface is small (Fig. 1 (a)) and that there is little drag between the fluid phases. In contrast, flows in high-permeability porous media are characterized by a complex interaction between capillary, gravity, viscous, and inertial forces (Dullien, 1992; Blunt, 2017; Davit and Quintard, 2018). Capillary effects may no longer dominate, and the capillary, Bond, and Weber numbers may be large. The distribution of fluids in the pore space can be schematically decomposed in two modes, even though the reality is often a lot more complex. Either the non-wetting fluid is continuous and flows in the center of the pores surrounded by the wetting fluid flowing as a thin film in contact with the solid (Fig. 1 (b)), or the non-wetting fluid is discontinuous and flows in the center of the pores as droplets or ganglias (Fig. 1 (c)). In both cases, the surface area between the fluids is large and the drag forces between the fluids may be non-negligible compared with the fluid-solid drag forces. This is in strong contrast with capillarity-dominated flow and it is of major importance since modeling of the drag forces is mandatory to build a comprehensive macroscopic model of the flow.

1.1. Generalized Darcy law with coupling

Models used to describe two-phase flows in porous media are often based on a direct extension of Darcy's equations for one-phase flow (Wyckoff and Botset, 1936; Muskat, 1938). This generalization is based upon introducing relative permeabilities, which can be understood as describing the impact of the division of the pore space between the fluids. Each fluid phase acts as a supplementary "solid" regarding the other one and no exchange between the phases is taken into account explicitly (Dullien, 1992; Blunt, 2017).

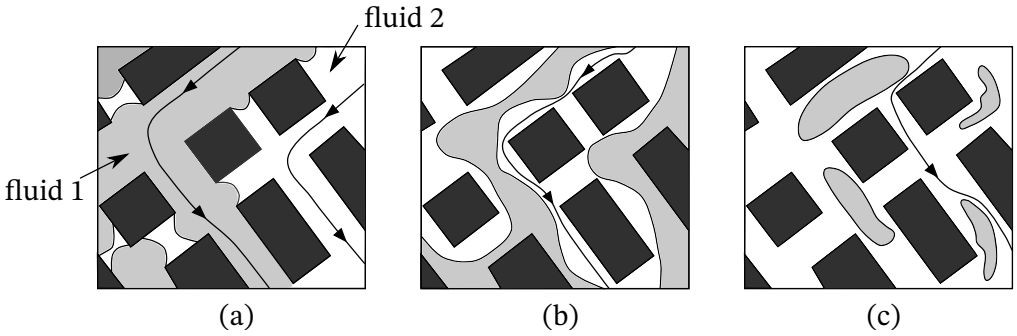

Figure 1: Schematics of example distributions of fluids in a 2D porous network with the solid phase in black, the non-wetting fluid (fluid 1) in light gray, and the wetting fluid (fluid 2) in white, (a) the two fluids are flowing in different channels separated by numerous meniscus and the fluid-fluid interface extent is small, (b) the wetting and non-wetting fluids are flowing together in most of the pores as two continuous streams, and (c) both fluids are flowing together in most of the pores and the non-wetting phase is discontinuous - Figure adapted from Dullien (1992).

Consequently, it is commonly assumed that the relative permeability for a given fluid pair only depends on the saturation (Brooks and Corey, 1964; Van Genuchten, 1980), even though the relative permeabilities may also depend on the capillary number (Li et al., 2005), the flow regime (Avraam and Payatakes, 1995; Bianchi Janetti et al., 2017), the viscosity ratio (Yuster et al., 1951; Ehrlich, 1993; Yiotis et al., 2007) and other properties such as wettability (Morrow et al., 1973; Anderson et al., 1987; Li et al., 2005). Since the early 1980s, much work has aimed at improving the generalized Darcy equations on a sound physical basis. Using upscaling techniques, several authors have proposed additional coupling terms that correspond to drags at the fluid-fluid interface and yield coupling permeability tensors (Marle, 1982; Auriault and Sanchez-Palencia, 1986; Whitaker, 1986; Lasseux et al.,

1996). The importance of these coupling terms in the overall flow process remains unclear (Ayub and Bentsen, 1999). These additional terms can be calculated analytically in a two-phase annular cocurrent flow in a cylindrical capillary tube and are of the same order of magnitude as the dominant relative permeabilities (Bacri et al., 1990). In this theoretical configuration the phase distribution does not depend on the tube radius, i.e., permeability. However, other studies considering more realistic configurations, for which the surface between fluids was smaller, concluded that coupling terms should not be as important (Scott et al., 1953; Rakotomalala et al., 1995; Ayodele, 2006). As explained above, this can be linked to the capillarity effect being important, and this effect may be related indirectly to the use of media with sufficiently low permeabilities. Zarcone and Lenormand (1994), Dullien and Dong (1996), and Ramakrishnan and Goode (2015) directly measured the coupling permeability terms in natural media by performing steady-state cocurrent two-phase flows. Rose (1988) proposed indirectly measuring the coupling relative permeability terms by performing two different types of experiments. This technique was also used for both cocurrent and countercurrent experiments (Bourbiaux et al., 1990; Bentsen and Manai, 1993). These authors (apart from Zarcone and Lenormand) found that the coupling relative permeabilities are significant. Using two different experiments raises questions on interpretation, in terms of a unique set of relative permeabilities and coupling terms, hence the existence of some confusion about the dependence of coupling terms with other physical parameters. In debris-bed cooling studies or flows in trickle-bed reactors, for which the porous media is highly permeable, several projects have shown that including closure terms

for the drag force between fluids can better predict measured pressure loss (Schmidt, 2007; Attou et al., 1999). Recently, Clavier et al. (2017) performed experiments of inertial two-phase flows in coarse non-consolidated porous media and proposed constitutive models for the coupling. They were motivated to introduce coupling terms after observing that phases were both flowing within the same pore-space due to the medium's high permeability. However, in most cases, it is impossible to know from the experiments which type of flow regime dominates at the pore-scale and therefore what is the exact link between the physics at the pore-scale and the macro-scale model.

1.2. Hele Shaw cell

Micromodels can be used to better understand the physics of two-phase flows in porous media (Karadimitriou and Hassanizadeh, 2012), for example, transitions between flow regimes or the onset and development of displacement instabilities (Lenormand et al., 1988; Zhang et al., 2011; Horgue et al., 2013). These apparatuses were used to measure the relative coupling permeabilities for different flow regimes (Avraam and Payatakes, 1995) or study the impact of the fluid-fluid drag on the flow characteristics (Heshmati and Piri, 2018; Roman et al., 2019). Rothman (1990) used numerical simulations in a 2D micromodel geometry at large capillary numbers and found that coupling permeabilities are comparable in magnitude with the case of the annular flow in a capillary tube. Fig. 2 shows Rothman's results along with some of the previously mentioned results on relative coupling permeabilities. Given the potential impact of permeability, i.e., characteristic pore length, on phase distribution and hence coupling terms, we also added to the legend of this figure the estimated order of magnitude of the permeability.

Hele-Shaw cells are one of the simplest examples of micromodels as they consist of two parallel plates forming a thin gap in which the fluids can flow. Many studies have focused on the displacement of bubbles and droplets in such cells (Maxworthy, 1986; Maruvada and Park, 1996; Kopf-Sill and Homsy, 1988) and the stability of the fluid front during the displacement of a fluid by another less viscous fluid (Saffman and Taylor, 1958; Bensimon, 1986; Meiburg and Homsy, 1988; Jackson et al., 2017; Cueto-Felgueroso and Juanes, 2014). The governing flow equations are analogous to Darcy's equation, therefore several studies used Hele-Shaw cells to gain insight about two-phase flow in porous media (Stokes et al., 1986; Homsy, 1987; Liu et al., 2019).

1.3. Outline of the study

In this work, we focus on immiscible cocurrent flow in a modified Hele-Shaw flow cell with obstacles to better capture the physics of porous media flows. We study numerically the influence of the intrinsic permeability on the fluid-fluid and fluids-solid drags for different capillary numbers. To do so, we use a diffuse interface for interface resolving method (Level Set), validated against a Boundary Element Method (BEM) code. The key idea is to vary the thickness of the flow cell to change the permeability without affecting the in-plane geometry. The objective is to quantify the importance of the fluid-fluid drag in two-phase flows in microfluidic devices, and by extension in highly permeable porous media models. In particular, we focus on film-flow regimes; common in highly permeable porous media.

The manuscript is organized as follows. The volume-averaged flow equations are derived in Section 2, starting from the 3D flow equations, and then depth-averaged to exhibit a permeability-like term that allows to control the

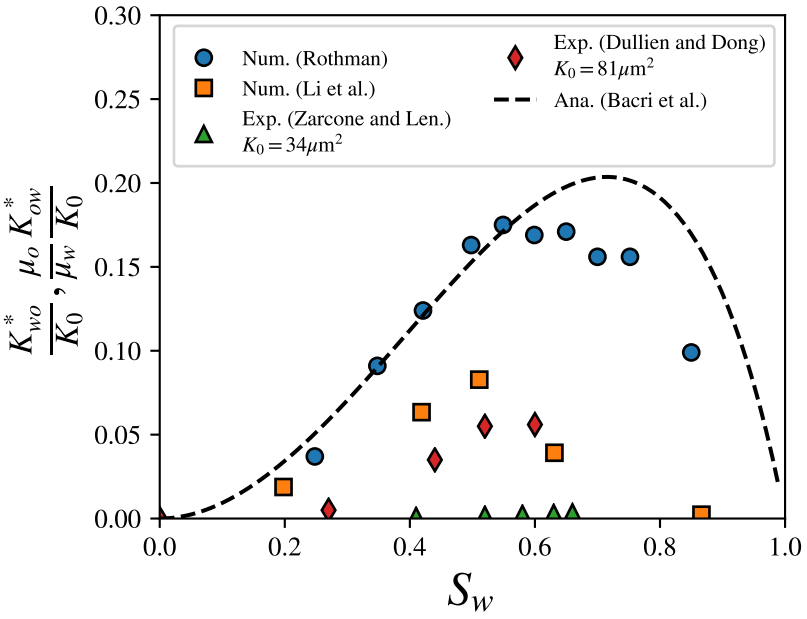

Figure 2: Normalized relative permeabilities for coupling K^*_{ij} as a function of the wetting-fluid saturation S_w from experimental work (Dullien and Dong, 1996; Zarcone and Lenormand, 1994), numerical simulations (Rothman, 1990; Li et al., 2005) and analytical solution for a steady-state annular two-phase flow in a circular capillary tube (dashed line) (Bacri et al., 1990). The theoretical capillary tube case provides an upper limit in terms of permeability and extent of the interfacial surface area between the fluids.

fluid-solid drag. In Section 3, the numerical method is introduced as well as the initial boundary value problem and the mesh convergence study. In Section 4, we present the results, the main ones concern the analysis of the drag forces at the different interfaces as a function of the gap thickness between the plates.

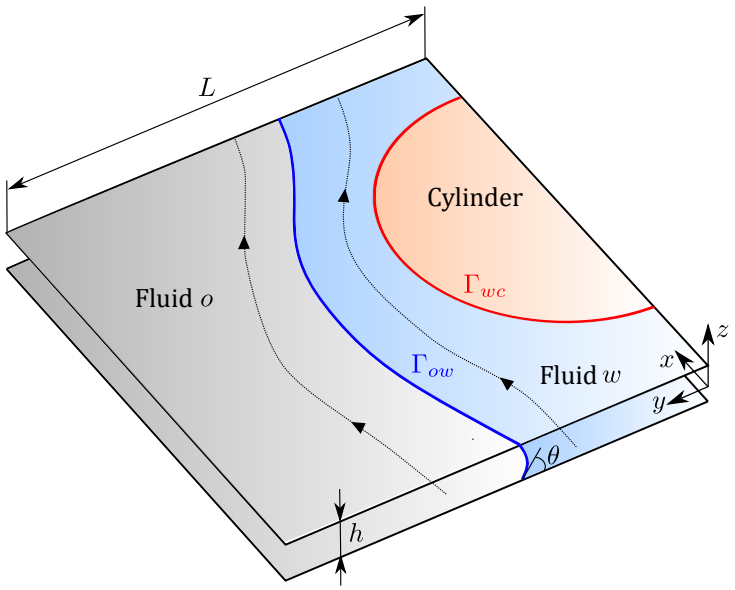

Figure 3: Schematic view of a cocurrent two-phase flow in a Hele-Shaw cell parallel to the $x-y$ plane with a solid obstacle of circular cross-section. L is the transverse dimension of the cell and h is the gap between plates. The boundary between the wetting-fluid w and the cylinder (in red) is noted Γ_{wc} and the boundary between the two fluids (in blue) is noted Γ_{ow}. No dynamic films along the plates are considered here. θ stands for the non-zero contact angle between the two fluids and the plates.

2. Pore-scale, depth-averaged and volume-averaged flow equations

In this section, we present the derivation of the averaged flow equations for cocurrent two-phase flows in a Hele-Shaw cell with a solid-phase obstacle of circular cross-section (Fig. 3). We start from the three-dimensional Stokes equations. Then, we average the momentum equations spatially to derive the unclosed form of the macroscopic momentum transport equations.

2.1. Pore-scale flow equations

Three-dimensional continuity and Stokes equations for a Newtonian fluid in the absence of external forces read, respectively,

$$\nabla^* \cdot \mathbf{u} = 0, \qquad -\nabla^* p + \mu \nabla^{*2} \mathbf{u} = 0, \tag{1}$$

where the superscript * indicates that the derivative operators are three-dimensional.

2.2. Depth-averaged flow equations

The starting point is to consider an apparatus such as the one depicted in Fig. 3, for which h is very small compared to the transverse length of the cell. It follows that the z-component of the velocity can be neglected (Guyon et al., 1994), at least sufficiently far away from the obstacle. In consequence, the three-dimensional velocity is

$$\mathbf{u} = (u(x,y,z), v(x,y,z), 0)^T = (\bar{u}(x,y)f(z), \bar{v}(x,y)f(z), 0)^T, \tag{2}$$

where we introduce the depth-averaged, two-dimensional, velocity vector defined as $\bar{\mathbf{u}} \equiv \frac{1}{h}\int_{-h/2}^{h/2} (u(x,y,z), v(x,y,z))^T \, \mathrm{d}z$. The in-plane version of Eq. 1 then reads

$$\nabla \cdot \bar{\mathbf{u}} = 0, \qquad -\nabla p + \mu \left(\nabla^2 \bar{\mathbf{u}} + \bar{\mathbf{u}} f'' \right) = 0. \tag{3}$$

where del is now used as a 2D operator. From the condition $\int_{-h/2}^{h/2} f(z)\mathrm{d}z = h$, arising from the definition of the depth-averaged velocity, along with the no-slip boundary condition at $z \pm h/2$, we find that $f(z) = \frac{3}{2}(1 - 4\frac{z^2}{h^2})$. Then,

$$\nabla \cdot \bar{\mathbf{u}} = 0, \qquad \mu \left(\nabla^2 \bar{\mathbf{u}} - k^2 \bar{\mathbf{u}} \right) = \nabla p, \tag{4}$$

are the continuity and momentum transport equations for the depth-averaged flow of one fluid with $k = \sqrt{12}/h$. Nagel and Gallaire (2015) showed that the velocity profile for a one-phase 3D flow in a rectangular channel is correctly reproduced with the depth-averaged model up to aspect ratios $h/L = 1$. We conducted a similar study in Appendix A, as the solid obstacles are likely to locally disturb the velocity field. We observed a slight deviation between depth-averaged 2D and 3D flows, even for small gaps, which can be attributed to the wall of the cylinders. This discrepancy does not increase with the gap, and the depth-averaged model is effective even for gaps as large as $h/L = 2$.

These depth-averaged equations have to be written for each fluid, and boundary conditions at the fluid-fluid interfaces are required to close the problem. Continuity of the depth-averaged velocities across the interface and a jump of the interface normal stress are sufficient conditions if surface tension is constant along the interface. These conditions are expressed as (Park and Homsy, 1984)

$$\bar{\mathbf{u}}_o - \bar{\mathbf{u}}_w = 0 \text{ at } \Gamma_{ow}, \tag{5}$$

$$(\bar{\sigma}_w - \bar{\sigma}_o) \cdot \mathbf{n}_{ow} = \gamma \left(\frac{\pi}{4} \kappa_{\parallel} + \frac{2}{h} \cos\theta \right) \mathbf{n}_{ow} \text{ at } \Gamma_{ow}, \tag{6}$$

where $\bar{\sigma}_i = -p_i \mathbf{I} + \mu_i (\nabla \bar{\mathbf{u}}_i + (\nabla \bar{\mathbf{u}}_i)^T)$ is the in-plane stress tensor of fluid i, $\mathbf{n}_{ow}$ is the in-plane normal vector at the fluid interface pointing toward the fluid w, γ is the surface tension, $\kappa_{\parallel}$ is the in-plane interface curvature and θ denotes the contact angle between the fluids interface and the plates (Fig. 3). The meniscus in the z-direction is approximated as a half-circle of radius $h/2$ and the $\pi/4$ correction for the in-plane curvature was derived by Park and

Homsy (1984). In Eq. 6, we neglected the additional terms that pertain to the formation of the dynamic film and scale non-linearly with the capillary number. We rather considered a non-zero contact angle, which minimizes the dynamic film left behind the meniscus.

2.3. Volume-averaged flow equations

Here, we proceed to the spatial averaging of the in-plane momentum transport equations, following the volume averaging method. This method has been largely employed for creeping two-phase flows at pore scale, either in its traditional acceptance (Whitaker, 1986; Lasseux et al., 1996; Chen et al., 2019) or with additional entropy relation, that is the thermodynamically constrained averaging theory (TCAT) (Gray and Miller, 2005, 2014). We recall that all the flow variables and differential operators have components only in the transverse direction. According to the volume averaging framework (Whitaker, 1999) and recalling that Eq. 4 are two-dimensional, the traditional averaging theorem for the depth-averaged quantity $\bar{\omega}_i$ associated with the fluid i reads

$$\langle \nabla \bar{\omega}_i \rangle = \nabla \langle \bar{\omega}_i \rangle + \frac{1}{S} \int_{\Gamma_{ic}} \mathbf{n}_{ic} \bar{\omega}_i \, \mathrm{d}\Gamma + \frac{1}{S} \int_{\Gamma_{ij}} \mathbf{n}_{ij} \bar{\omega}_i \, \mathrm{d}\Gamma, \tag{7}$$

where,

$$\langle \bar{\omega}_i \rangle = \frac{1}{S} \int_{S_i} \bar{\omega}_i \, \mathrm{d}S, \tag{8}$$

is the superficial surface average and S is the surface of a representative elementary cell. Applying the superficial surface average of Eq. 4 along with the averaging theorem and using traditional length-scale arguments (Whitaker, 1999) we obtain

$$\nabla \cdot \langle \bar{\mathbf{u}}_i \rangle = 0, \quad i = o, w, \tag{9a}$$

$$\frac{1}{S}\int_{\Gamma_{ic}} \mathbf{n}_{ic}\cdot\left(-p_i\mathbf{I}+\mu_i\left(\nabla\bar{\mathbf{u}}_i+(\nabla\bar{\mathbf{u}}_i)^T\right)\right)\,\mathrm{d}\Gamma+$$
$$\frac{1}{S}\int_{\Gamma_{ij}} \mathbf{n}_{ij}\cdot\left(-p_i\mathbf{I}+\mu_i\left(\nabla\bar{\mathbf{u}}_i+(\nabla\bar{\mathbf{u}}_i)^T\right)\right)\,\mathrm{d}\Gamma-$$
$$\mu_i k^2\langle\bar{\mathbf{u}}_i\rangle=\varepsilon_i\nabla\langle p_i\rangle^i+\langle p_i\rangle^i\nabla\varepsilon_i,\quad i,j=o,w,\ i\neq j, \tag{9b}$$

where $\mathbf{I}$ is the 2×2 identity matrix and $\langle p_i\rangle^i\,(\langle p_i\rangle^i=\langle p_i\rangle/\varepsilon_i)$ is the intrinsic surface average pressure of fluid i, with ε_i the volume fraction of fluid i. The first integral is the drag force exerted upon the obstacle boundary by fluid i and the second integral pertains to the drag force exerted upon fluid j by fluid i. Here, we consider that the contour of the fluid-fluid interface in the $x-y$ plane can be identically translated along the z-direction, which is an approximation since the meniscus is a half-circle for small h/L ratio. If the variation of the saturation in space is negligible and acknowledging that, as illustrated in Fig. 3, only the wetting fluid w is in contact with the obstacle, a more compact form of Eq. 9b reads

$$0=-\varepsilon_w\nabla\langle p_w\rangle^w-\mu_w k^2\langle\bar{\mathbf{u}}_w\rangle+\mathbf{d}_{wc}+\mathbf{d}_{wo}, \tag{10a}$$
$$0=-\varepsilon_o\nabla\langle p_o\rangle^o-\mu_o k^2\langle\bar{\mathbf{u}}_o\rangle+\mathbf{d}_{ow}, \tag{10b}$$

where, $\mathbf{d}_{ij}$ ($\mathbf{d}_{ij}=\frac{1}{S}\int_{\Gamma_{ij}}\boldsymbol{\sigma}_i\cdot\mathbf{n}_{ij}\mathrm{d}\Gamma$) denotes the drag forces per unit surface area exerted upon phase j by phase i and which must be computed or modeled to obtain closed macroscopic equations.

3. Direct numerical simulations

In this section, we introduce the standard Level Set method to capture the moving free interface between the fluids, along with the flow equations,

Drag of... upon...	Fluid o	Fluid w
Plates	$-\mu_o\langle\bar{\mathbf{u}}_o\rangle\frac{12}{h^2}$	$-\mu_w\langle\bar{\mathbf{u}}_w\rangle\frac{12}{h^2}$
Obstacle	-	$\mathbf{d}_{wc}$
Fluid o	-	$\mathbf{d}_{wo}$
Fluid w	$\mathbf{d}_{ow}$	-

Table 1: Summary of drag force terms involved in the averaged momentum transport equation for two-phase flow in a Hele-Shaw cell ($k = \sqrt{12}/h$).

both solved with the finite element solver Comsol Multiphysics®. In the following, we are working on the direct calculation of each drag force terms summarized in Table 1.

3.1. Equations

The Level Set method is a Eulerian method that easily handles topological phase changes, in contrast with Lagrangian methods. Here, the fluid phases are identified with a phase color function that goes smoothly from 0 to 1 across the fluid interface with the manifold defined as the iso-level $\phi = 0.5$. Transport of the level set function ϕ is governed by

$$\frac{\partial\phi}{\partial t} + \nabla\cdot(\bar{\mathbf{u}}\phi) = \tau\nabla\cdot\left(\psi\boldsymbol{\nabla}\phi - \phi(1-\phi)\frac{\boldsymbol{\nabla}\phi}{|\nabla\phi|}\right), \tag{11}$$

where $\bar{\mathbf{u}}$ is the depth-averaged velocity field and τ and ψ are two numerical parameters that control the diffuse interface thickness and the amount of initialization of ϕ function, respectively (Olsson and Kreiss, 2005). The same method has been used by Bashir et al. (2014) to reproduced the droplet

generation in a 2D T-junction micromodel. We investigated the accuracy of the implicit definition of the interface and the proper value of the initialization parameter by comparing the interface position to a boundary element method (Nagel and Gallaire, 2015). We found that the inlet velocity is a good value (it is often recommended to start with the maximum magnitude of the velocity expected at the fluid-fluid interface as a first guess). We chose for τ a standard value (Olsson et al., 2007) depending on the maximum size of mesh elements (i.e., $\tau = \max(\Delta x)/2$). The governing flow equations read

$$0 = \nabla \cdot \bar{\mathbf{u}} \tag{12a}$$

$$0 = -\nabla p + \mu(\phi)\left(\nabla^2 \bar{\mathbf{u}} - \frac{12}{h^2}\bar{\mathbf{u}}\right) + \gamma\left(\frac{\pi}{4}\nabla \cdot \left(\frac{\boldsymbol{\nabla}\phi}{|\boldsymbol{\nabla}\phi|}\right) - \frac{2}{h}\right)\delta(\phi)\mathbf{n}, \tag{12b}$$

where δ is the Dirac delta function localized on the interface and $\mathbf{n}$ denotes the unit normal to the interface, respectively defined as,

$$\delta(\phi) = 6\,|\boldsymbol{\nabla}\phi|\,|\phi\,(1+\phi)|\,, \quad \text{and} \quad \mathbf{n} = \frac{\boldsymbol{\nabla}\phi}{|\boldsymbol{\nabla}\phi|}. \tag{13}$$

We introduce the following reference and dimensionless quantities,

$$\bar{\mathbf{u}} = \bar{\mathbf{u}}' \times U_r,\ p = p' \times \frac{\mu_r U_r}{L},\ \mathbf{x} = \mathbf{x}' \times L, \tag{14}$$

and the dimensionless continuity and momentum transport equations are

$$0 = \nabla' \cdot \bar{\mathbf{u}}' \tag{15a}$$

$$0 = -\nabla' p' + \frac{\mu(\phi)}{\mu_r}\left(\nabla'^2 \bar{\mathbf{u}}' - \frac{12}{(h/L)^2}\bar{\mathbf{u}}'\right) + \frac{\gamma}{\mu_r U_r}\left(\frac{\pi}{4}\nabla' \cdot \left(\frac{\boldsymbol{\nabla}'\phi}{|\boldsymbol{\nabla}'\phi|}\right) - \frac{2}{h/L}\right)\delta'(\phi)\mathbf{n}, \tag{15b}$$

with $\delta'(\phi) = 6\,|\boldsymbol{\nabla}'\phi|\,|\phi\,(1+\phi)|$. We therefore have three dimensionless numbers: the viscosity ratio $M(\phi) = \frac{\mu(\phi)}{\mu_r}$, the capillary number $Ca^{-1} = \frac{\gamma}{\mu_r U_r}$ and the aspect ratio $h^* = h/L$.

3.2. Geometry, boundary conditions and simulation parameters

Our macroscopic model is a Hele-Shaw cell with solid obstacles having cylindrical cross-section. This system is subdivided into seven unit-cell (UC) subdomains encompassing one obstacle, as depicted in Fig. 4. Seven were chosen to minimize computational costs based on the observation that, at steady-state, the impact of inlet and outlet boundaries is nearly limited to a single unit-cell, and that the phase distribution is quasi-periodic for the remaining unit cells (see Sec. 4.1). Taking advantage of the symmetry, we solved only for the upper half of a row. Each fluid flows from left to right (x-direction) and the inlet boundary conditions for both fluids are a constant normal inlet velocity u_i. The outlet boundary condition for the flow is a reference pressure. These boundary conditions are summarized in Table 2. We choose the sum of the inlet velocity of both fluids as the reference velocity, so the dimensionless inlet velocities can be expressed as a fractional flow f_f,

$$f_f = \frac{u_w}{U_t}, \quad u_o = 1 - f_f, \quad \text{with} \quad U_t = u_w + u_o. \tag{16}$$

The non-wetting fluid's viscosity was taken as the reference viscosity and the respective values of the dimensionless parameters are given in Tab. 3. Contact angle between fluid o (non-wetting) and the solid obstacles is $\theta = 0°$. The initialization parameter value is equal to the maximum inlet velocity value, which yields maximum accuracy. As a reference, we conducted numerical simulations of one-phase flows and found that the gap range used in this study corresponds to intrinsic permeabilities between 1.5×10^4 and 40 darcy.

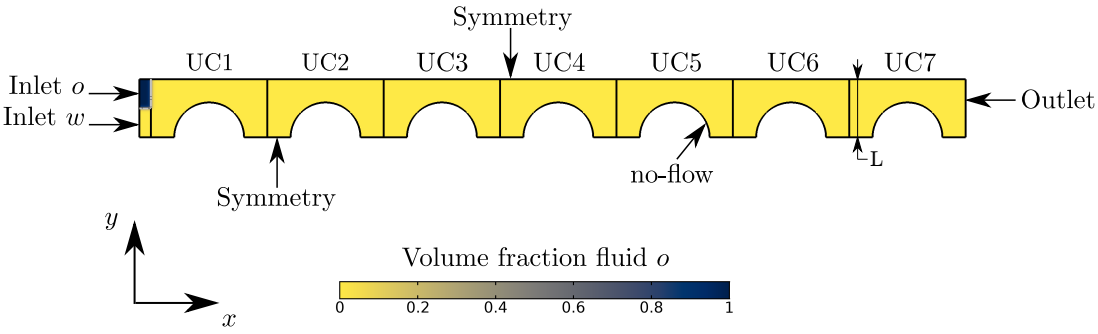

Figure 4: Schematics of geometry and initial conditions. We considered the upper half of an array of seven cylindrical obstacles inside seven cuboids where both fluids are injected from left to right. Initially, the model was saturated with wetting fluid (red), and the width L of one Unit Cell (UC) is 5×10^{-4} m. Symmetry boundary conditions were used on both length sides and the no-flow boundary condition was imposed at the obstacle boundary.

Table 2: Boundary conditions for flow variables and the Level Set function (left) and simulation parameters.

Boundary	u	p	ϕ
Outlet	-	0	$\mathbf{n} \cdot \boldsymbol{\nabla} \phi = 0$
Inlet o	u_o	-	0
Inlet w	u_w	-	1

Table 3: Parameters used for the direct numerical simulations.

Parameters	Value	Physical parameter
$Ca = \frac{U_t \mu_o}{\gamma}$	from 5×10^{-1} to 2.5×10^{-2}	$2.2 \times 10^{-3} \lesssim \gamma \lesssim 4.5 \times 10^{-2}$ mN/m
$M_w = \frac{\mu_w}{\mu_o}$	1	$\mu_o = 10^{-3}$ Pa.s
$f_f = \frac{u_w}{U_t}$	1/4	$U_t = 8 \times 10^{-4}$ m/s
$h^* = h/L$	from 5 to 1/20 and 2D case	$L = 5 \times 10^{-4}$ m

3.3. Mesh sensitivity analysis

Here, we study the mesh convergence of drag forces and averaged velocity. Three cases were investigated : (*case A*) $Ca = 1.25 \times 10^{-1}$, $h^* = 1/4$, (*case B*) $Ca = 2.5 \times 10^{-2}$, $h^* = 1/10$ and (*case C*) $Ca = 5 \times 10^{-1}$, $h^* = 5$. Other parameters are kept constant, i.e., $f_f = 0.25$ and $M = 1$. In Fig. 5 the results are normalized with respect to those obtained from the finest mesh and are given as a function of the relative number of mesh elements in the whole model, starting from 1000 triangular mesh elements as a basis. The fluid-fluid interface position for three different meshes is given in Fig. 5 (d) for the fourth unit-cell (UC4) and *case B*. We found that the drag terms are not very sensitive to the mesh density and that the interface between the fluids also converges relatively quickly. Therefore, in the following simulations, we use a mesh made of 4.3×10^4 elements.

4. Results

The results of the cocurrent two-phase flows in the aforementioned micro-model are organized as follows. We describe the flow regime observed with

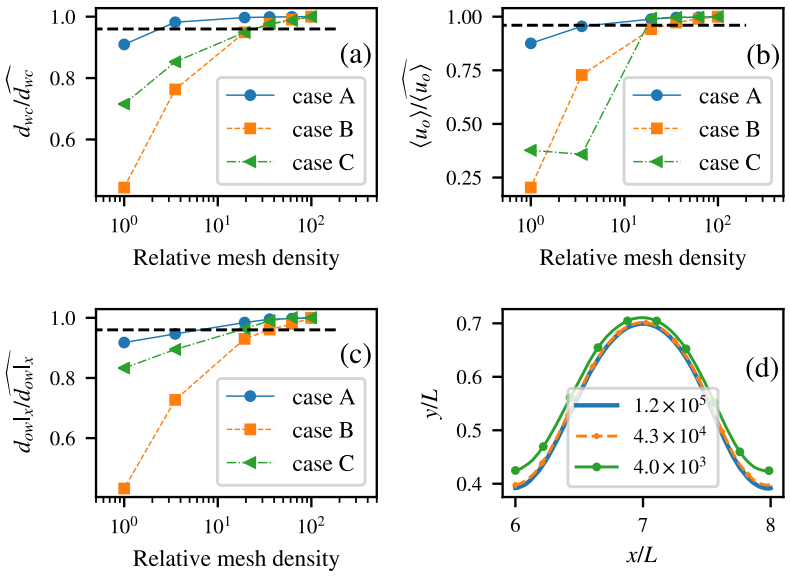

Figure 5: Mesh convergence study of (a) drag force exerted upon the obstacle, (b) intrinsic average velocity of fluid o (c) drag force exerted upon the fluid-fluid boundary and (d) position of the fluid-fluid interface for case B and for different number of mesh elements. All the results are normalized with respect to the result obtained with the finer mesh, denoted with $\widehat{symbol}$, at steady-state and in UC4. Case A refers to $Ca = 1.25 \times 10^{-1}$, $h^* = 1/4$, case B refers to $Ca = 2.5 \times 10^{-2}$, $h^* = 1/20$ and case C refers to $Ca = 5 \times 10^{-1}$, $h^* = 5$. Other flow parameters are constant, $f_f = 0.25$ and $M = 1$. In the following we use a mesh made of 4.3×10^4 elements.

the selected parameters. The regime is fundamental as it drives the extent of the interfacial surface area between the fluids and therefore the amount of fluid-fluid drag. The saturation and the fluid-fluid interface are presented as a function of the gap thickness and capillary numbers. Then we discuss the effect of the flow confinement, i.e. the permeability, on the velocity and pressure fields. The main section discusses the value of each drag terms presented

in Eq. 10.

4.1. Flow regimes and fluid saturations

As previously discussed, the continuity of the non-wetting phase, and thus the flow regime, may vary in such systems. Here, the continuity of the non-wetting fluid, depends, among other things, on the fractional flow f_f and the ratio of the transverse injection lengths of each fluid y_i/L. We observed breakup of the non-wetting fluid for high fractional flow and small section of injection of this fluid, as shown in Fig. 6. The state diagram was obtained for $Ca = 2.5 \times 10^{-2}$ and a thin gap $h^* = 1/20$, which is the most favorable case for phase breakage, due to greater capillary effects, among the parameters we used. We focus on the film-flow regime in the following, so we chose to perform all the simulations with a low fractional flow ($f_f = 0.25$) and a medium inlet section ($y_o/L = 0.5$). For these parameters, we observed that the two fluids remain continuous at all times and for the entire range of tested capillary numbers and gap thickness, as described in Table 3. The interface between the fluids becomes stationary and steady-state is reached for every capillary number and values of gap thickness.

As an example, Fig. 7 shows the initial, intermediate, and final configurations of the fluid distribution for $Ca = 1.25 \times 10^{-1}$ and $h^* = 1/8$. The fluid-fluid interface is periodic on the five central unit cells at steady-state whereas the interface is slightly deformed at the inlet and outlet cells, under the influence of boundary conditions.

The penetration of the non-wetting fluid shown in Fig. 7 does not result from an unstable displacement, i.e. viscous fingering, since both fluids have the same viscosity. Here, non-wetting phase break-up could have occurred

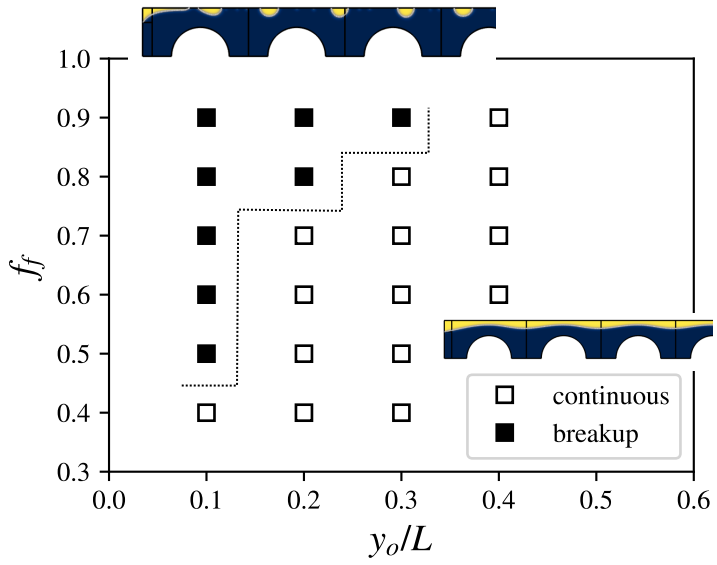

Figure 6: State diagram of the non-wetting phase (in yellow) connectivity during cocurrent two-phase flows in our modified Hele-Shaw cell. The results are given as a function of the fractional flow and the dimensionless inlet length of the non-wetting fluid y_o/L. Here, $h^* = 1/20$ and $Ca = 2.5 \times 10^{-2}$. Breakup of the non-wetting fluid occurred for high fractional flow and small dimension of the inlet.

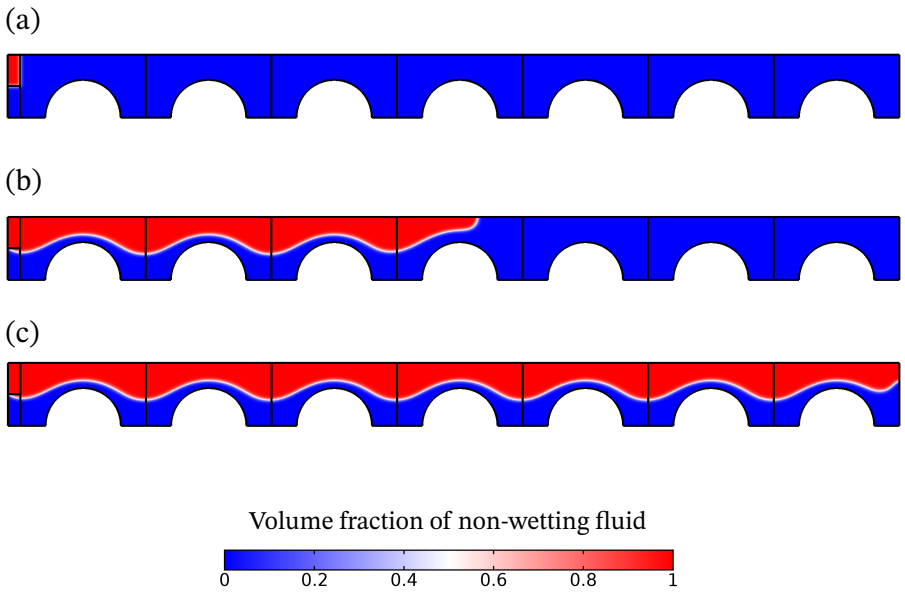

Figure 7: Fluids distribution along the upper half-row at (a) the initial time, (b) an intermediate time and (c) the final time (steady-state reached) for $Ca = 1.25 \times 10^{-1}$, $f_f = 0.25$, $M = 1$ and $h^* = 1/8$. At steady-state the fluid-fluid interface taken on the central unit cells is periodic whereas it is slightly deformed in the first and last UC under the influence of the boundary conditions.

either by snap-off phenomenon or because of the shear exerted by the wetting fluid. However, the pore throat is large and the fractional flow is low, which favors the continuity of the non-wetting fluid phase. The flow-regime observed is therefore a film-flow regime within the limit of the parameters chosen for this study.

Fig. 8 shows the wetting fluid saturation at steady-state as a function of the dimensionless gap between the plates and for different capillary numbers. Wetting fluid saturation at steady-state decreases, on average, from 0.6 to 0.4 as the dimensionless gap between the plates decreases from 5 to 1/20.

The results for the largest gaps are very close to the purely 2D results. The saturation fields insets in Fig. 8 indicate that the fluid-fluid interfaces are very similar for the thinnest gaps, whereas they differ significantly according to the capillary number for thicker gaps. This last point explains the different saturation we observed. Indeed, for low capillary numbers, the interface is flatter than for high capillary numbers, as shown in Fig. 9. Two configurations are possible, either the capillary number is high and the fluid-fluid interface is mostly translated toward the pore throat as the gap increases, or the capillary number is low enough that the fluid-fluid interface is deformed (flattened) and also pushed towards the pore throat for an increasing gap thickness. Another important feature that plays a role at the interfacial drag is the symmetry of the fluid-fluid interface, as can be seen from Fig. 9. The interface tends to be symmetric when the gap becomes very thin for any capillary number, and it also tends to be symmetric, whatever the gap, when the capillary number is large. These different fluid configurations might lead to substantial differences in the velocity and pressure fields, for example by forming a narrow channel with high local velocity, which would also impact the amount of drag.

4.2. Pressure and velocity fields

Fig. 10 shows the pressure field for selected values of capillary number and gap thickness. The main result here is that the pressure jump across the fluid-fluid interface is very difficult to distinguish for the largest value of the capillary number $Ca = 5 \times 10^{-1}$, especially for the thinnest gap. This is because the main pressure contribution to the pressure jump arises from the out-of-plane curvature and thus scales as h^{-1}, whereas the pressure gradient

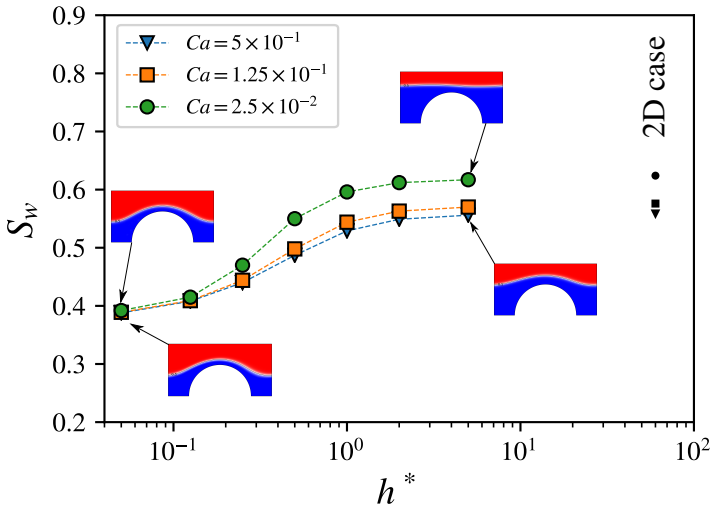

Figure 8: Fluid saturation at steady-state in UC4 as a function of the dimensionless gap and for different capillary numbers. Fields of the level-set function at steady-state in UC4 are given for the selected value of the dimensionless gap and $Ca = 1.25 \times 10^{-1}$. Wetting fluid hold-up increases for thicker gaps. The 2D limit case is given with plain black markers.

across the cell scales as h^{-2} for the very thin gap, for which the Darcean terms are expected to be dominant. In contrast, the pressure jump is visible for the smallest value of the capillary number $Ca = 2.5 \times 10^{-2}$. In this last case, we see that the pressure is higher in the non-wetting fluid, which is in agreement with the orientation of the out-of-plane meniscus.

Fig. 11 shows the velocity field, normalized with respect to the reference velocity, for the same parameters as for the pressure fields. The corresponding streamlines and the position of the fluid-fluid interface are also presented for three different cases. For the thinnest gap ($h^* = 1/20$), the velocity fields are alike regardless of the capillary number. In this case, the maximum velocity is

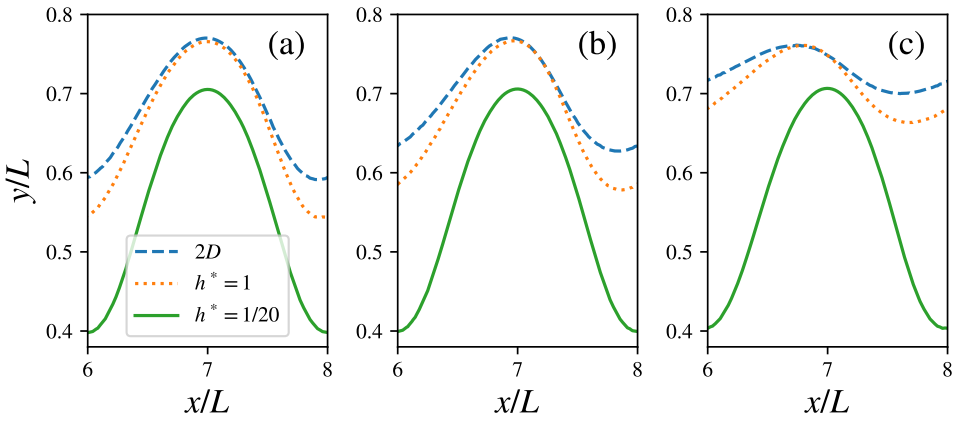

Figure 9: Comparison of the fluid-fluid interface at steady-state in UC4 for different dimensionless gaps between the plates. The interfaces are almost symmetric about the y-axis for a very thin gap for (a) $Ca = 5 \times 10^{-1}$ and (b) $Ca = 1.25 \times 10^{-1}$. The interfaces are flattenned for larger gaps for (c) $Ca = 2.5 \times 10^{-2}$. Here, $f_f = 0.25$ and $M = 1$).

reached in the center of the pore throat and between the fluid-fluid interface and the obstacle boundary. For the thickest gap, the velocity field depends on the capillary number. Either the capillary number is high and the maximum velocity is reached precisely in the center of the pore throat or the capillary number is low and the maximum velocity is slightly offset from the center overhang the fluid interface directly where it forms a narrower constriction. In this case, we also notice that recirculation cells develop in the wetting fluid. This observation is a direct manifestation of the momentum transfer between the two fluids (see also Alamooti et al. (2020)) and indicates that the fluid-fluid interface should not be treated similarly to fluid/solid boundaries, or at least not as a fixed wall. In the following, we study the drag force terms between phases and the effect of permeability and capillary number on them.

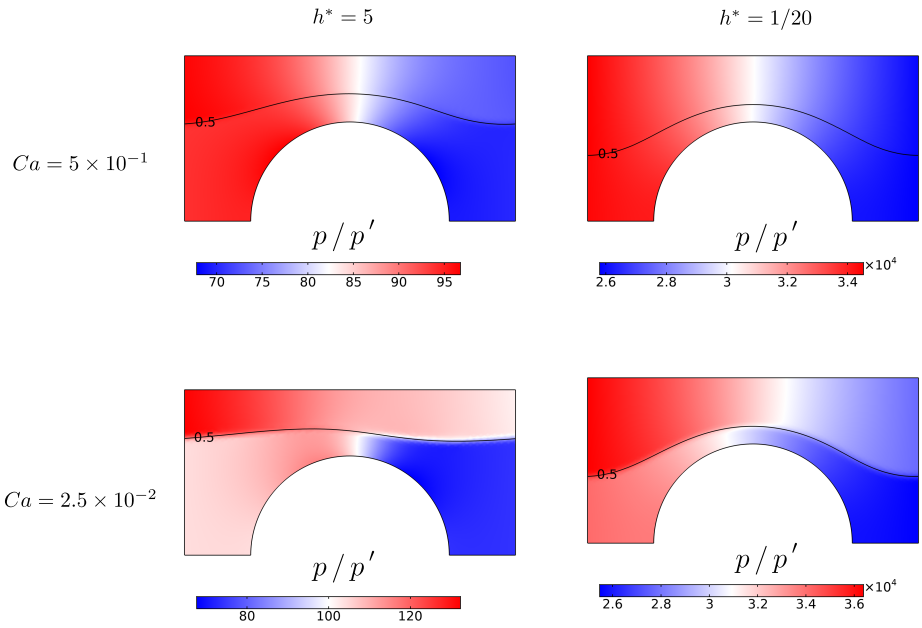

Figure 10: Comparison of the pressure field for two capillary numbers $Ca = 5 \times 10^{-1}$ (top row), $Ca = 2.5 \times 10^{-2}$ (bottom row) and two dimensionless gap thickness, with $h^* = 5$ (left column) and $h^* = 1/20$ (right column). The solid black line denotes the fluid-fluid interface given by the contour $\phi = 0.5$. Results in UC4 at steady-state for $f_f = 0.25$ and $M = 1$. The pressure jump across the fluid is not discernable for a high capillary number, regardless of the gap's thickness, as opposed to pressure fields for a small capillary number.

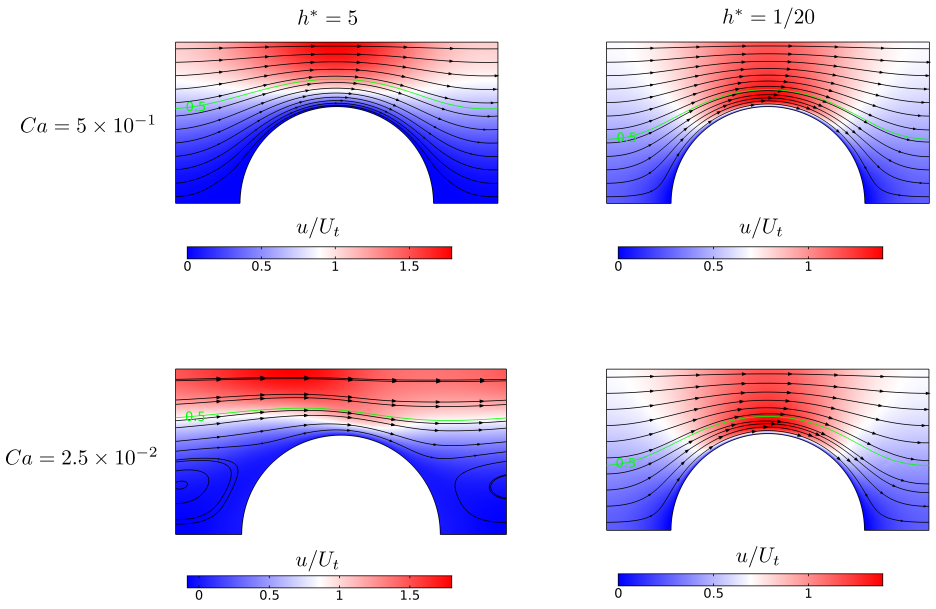

Figure 11: Comparison of the velocity field for two capillary numbers $Ca = 5 \times 10^{-1}$ (top row), $Ca = 2.5 \times 10^{-2}$ (bottom row) and two dimensionless gap thickness, with $h^* = 5$ (left column) and $h^* = 1/20$ (right column). The solid green line denotes the fluid-fluid interface given by the contour $\phi = 0.5$. Results in UC4 at steady-state for $f_f = 0.25$ and $M = 1$. Recirculation cells appeared for low capillary number and thin gaps, which illustrate the momentum transfer from the core fluid o to the wetting fluid w.

4.3. Drag forces between phases

We are only interested in the x-component of the drag forces, d_{ij}, because it is the main flow direction and we expect that $\partial_y p_i \ll \partial_x p_i$. We also know from the symmetry of the problem that the gradient of the average pressure in the y-direction is zero. We start from the sum of the superficial mean pressure drops, from Eqs. 10,

$$\underbrace{\partial_x \langle p_w \rangle + \partial_x \langle p_o \rangle}_{\partial_x P} = \underbrace{-\frac{12}{h^2}\left(\mu_w \langle u_w \rangle + \mu_o \langle u_o \rangle\right) + d_{wc}}_{d_s} + d_{ow} + d_{wo}, \tag{17}$$

with $\partial_x P$ the total pressure drop and d_s the sum of all fluid-solid drag forces. The two pressure drops are plotted against the dimensionless gap thickness for different capillary numbers in Fig. 12. Both mostly depend on the gap thickness. For large gaps $h^* \geq 1/2$, the pressure drops tend gently towards the smaller pressure drop obtained for 2D flow. For smaller gaps $h^* < 1/2$, the pressure drops scale as h^{-2}, the same as the drag upon the plates. We noticed that, if $d_{wo} \approx -d_{ow}$, then $\partial_x P \approx d_s$, recalling that d_{ij} stands for the x-component of the drag force $\mathbf{d}_{ij}$. To check whether this is the case, we calculated the following integral, from Eq. 6,

$$d_{wo} = -d_{ow} + \underbrace{\int_{\Gamma_{ow}} \gamma \left(\frac{\pi}{4}\kappa_{\parallel} + \frac{2}{h}\cos\theta\right) \mathbf{n}_{ow} \cdot \mathbf{e}_x \, \mathrm{d}\Gamma}_{I_c}. \tag{18}$$

Fig. 13 shows the integral I_c normalized with respect to the fluid-fluid drag. Ratio between I_c and d_{ow} is at a maximum (≈ 0.1) for the smaller Ca and $h^* = 1/4$, then it decreases for thinner gaps, since the fluid-fluid interface tends to be symmetric about the y-axis, thus $\int_{\Gamma_{ow}} \mathbf{n}_{ow} \cdot \mathbf{e}_x \, \mathrm{d}\Gamma$ tends to zero. In

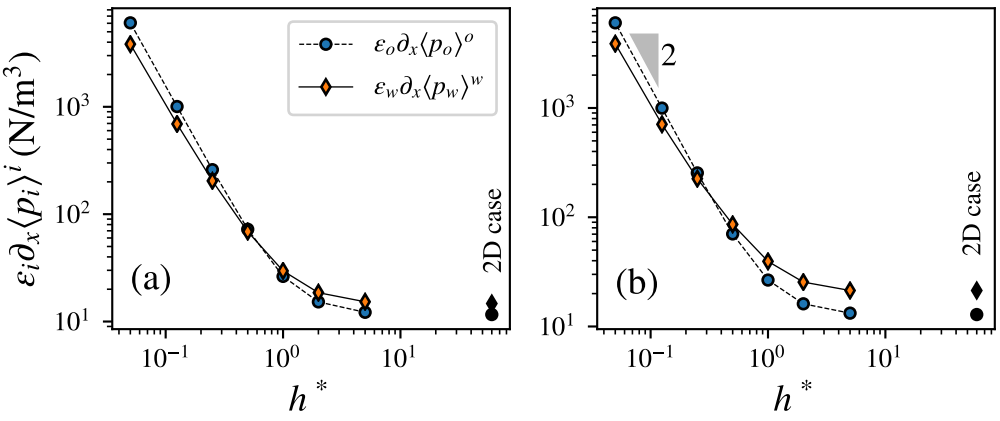

Figure 12: Pressure drop across the model as a function of the dimensionless gap thickness for each fluid. (a) $Ca = 5 \times 10^{-1}$ and (b) $Ca = 2.5 \times 10^{-2}$. Here, $M = 1$, $f_f = 0.25$ and the results are in UC4. The results from 2D Stokes equation are given with the black markers. The pressure drop scales as h^{-2} for thin gaps $h^* \leq 1/4$ for all values of Ca.

I_c, the contribution from the out-of-plane meniscus dominates by an order of magnitude over the contribution of the in-plane curvature for small gaps $h^* \leq 1/4$, whereas both contributions are equivalent for larger gaps. Consequently, the fluid-fluid drag contributions cancel each other in Eq. 17, $d_{wo} \approx -d_{ow}$ in the following and the total pressure drop is approximately equal to the sum of the fluid-solid drag.

Fig. 14 shows the relative part of each fluid-solid drag force in the total pressure drop ($\partial_x P$). For 2D flows, the total pressure drop is entirely due to the wetting fluid drag upon the cylinder. For very thin gaps, about half of the mean pressure drop is due to the drag upon the cylinder, whereas the other half is due to the drag upon the plates. In all cases, the total pressure drop can be approximated by the sum of all the fluid-solid drag forces, as

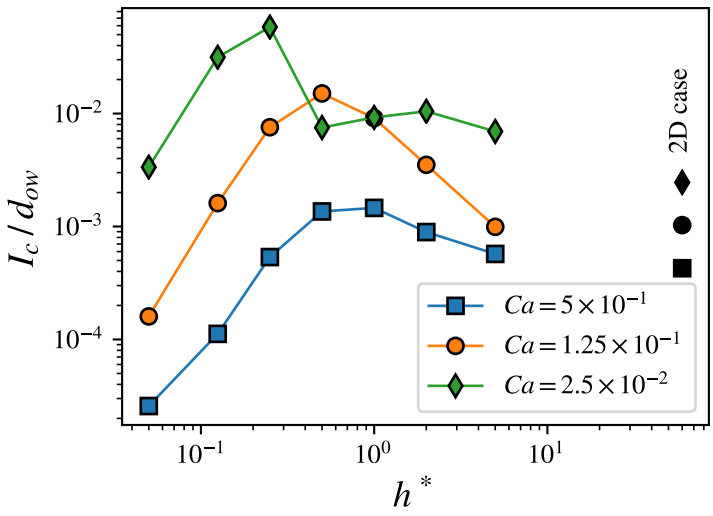

Figure 13: Value of the integral I_c in Eq. 18, non-dimensionalized by the fluid-fluid drag, as a function of the dimensionless gap thickness. Here, $M = 1$, $f_f = 0.25$ and the results are in UC4. The results from 2D Stokes equation are given with the black markers.

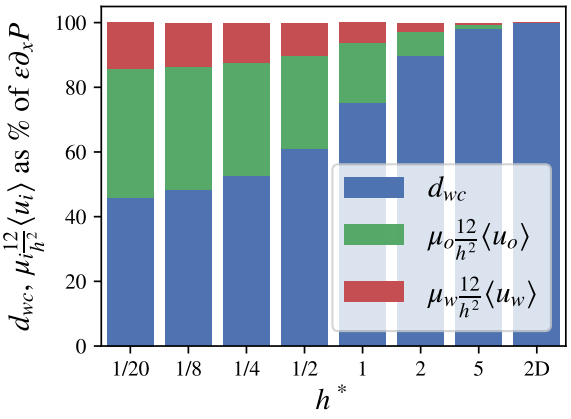

Figure 14: Part of the total mean pressure drop produced by the drag upon the obstacle and upon the plates by each fluid for different dimensionless gap thickness. Results are given for $Ca = 5 \times 10^{-1}$ only since the allocation is very alike for other value of Ca. Here, $M = 1$, $f_f = 0.25$ and the results are in UC4 at steady-state. The total pressure drop is the sum of the mean pressure gradient of each fluid ($\nabla P = \nabla\langle p_w \rangle + \nabla\langle p_o \rangle$).

predicted by Eq. 17.

We now turn to the fluid-fluid drag force. Fig. 15 shows the part of each drag force in the pressure drop of the non-wetting fluid and wetting fluid. Focusing on the fluid-fluid drag, we notice that its part in the pressure drop is not negligible, even for very thin gaps, since it reaches approximately 40% of $\partial_x \langle p_i \rangle$ for $h^* = 1/20$, whatever the value of Ca. This part increases for thicker gaps (i.e. for higher permeability) up to the maximum value reached for the 2D flow. As an example, the pressure drop of the non-wetting fluid is, logically, entirely due to the fluid-fluid drag force for a 2D flow. Now, looking at the other drags, we notice that the drag upon the obstacle is higher than the drag upon the plates, the former generates, at least, approximately 60% of the pressure drop of the wetting fluid. It is interesting to observe that

the relative part of each drag remains quite constant for thin gaps $h^* < 1/4$, which indicates that for thin gaps all the drag forces scales the same, and precisely scale as h^{-2}, as previously observed by looking at the pressure drops. A discrepancy is observable between the pressure drop and the sum of the drags for thick gaps and small Ca, due to the approximations when considering that the two drag forces are equal. Finally, the main findings here are that the fluid-fluid drag force is non-negligible compared to the fluid-solid drag forces and that the relative importance of this drag increases with the gap, therefore with the permeability. We also observe that the relative part of each drag is constant for very thin gaps $h^* \leq 1/4$. In the following paragraph, we present a scaling argument to explain this finding.

The limit case of very thin gaps is best described by Darcy's law. The pressure drag can be written as $d_{ij}^p = -\frac{1}{S}\int p_i \mathbf{n}_{ij} \cdot \mathbf{e}_x \, \mathrm{d}\Gamma$ and the viscous drag as $d_{ij}^\mu = \left(\frac{1}{S}\int \mu_i \nabla\langle u_i\rangle \cdot \mathbf{n}_{ij} \, \mathrm{d}\Gamma\right) \cdot \mathbf{e}_x$. Estimation of the pressure is given, in the thin-gap regime, by Darcy's law as $p \approx L\langle u\rangle\mu/h^2$. Since the viscous stress can be estimated as $\mu\langle u\rangle/L$, the ratio between these two terms scales as L/h, and the viscous drag is negligible in front of the pressure drag when $L/h \gg 1$. Now, the pressure term is applied on a contour of length L, so $d_f^p \approx \langle u\rangle\mu/h^2$. Consequently, the pressure drag at the fluid-fluid interface scales as the drag upon the plates. The features of the thin-gap regime, defined as $h^* \leq 1/4$, are (i) the pressure drag dominates over the viscous drag, which is negligible, and (ii) the pressure drag scales as the drag upon the plates, and the fluid-fluid drag is not negligible. All drag forces scale the same in this latter regime.

This scaling reasoning can be checked by looking at the pressure and

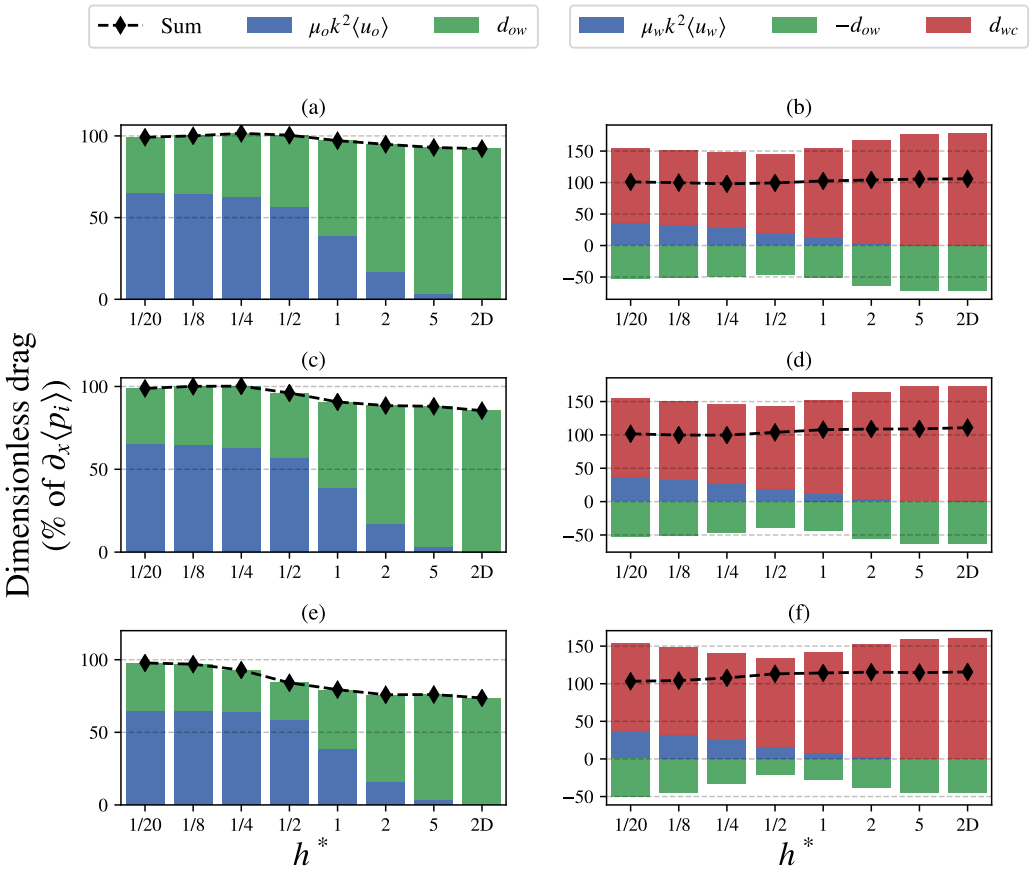

Figure 15: Part of the drag forces in the mean pressure gradient of a given fluid. Results are given for each dimensionless gap thickness and capillary number. (a) fluid o and (b) fluid w for $Ca = 5 \times 10^{-1}$, (c) fluid o and (d) fluid w for $Ca = 1.25 \times 10^{-1}$, (e) and (f) fluid o and w, respectively, for $Ca = 2.5 \times 10^{-2}$. The sum of all drag forces is given with the black markers. Here, $M = 1$, $f_f = 0.25$, and the results are in UC4 after steady-state was reached. The discrepancy for thick gaps and low Ca comes from the approximation made by considering that the fluid-fluid drag forces are equal.

viscous drag in the fluid-fluid drag force

$$d_{ij} = \underbrace{\frac{1}{S}\int_{\Gamma_{ij}} -p_i \mathbf{n}_{ij}\cdot\mathbf{e}_x \,\mathrm{d}\Gamma}_{d_{ij}^p} + \underbrace{\frac{1}{S}\int_{\Gamma_{ij}} \mathbf{n}_{ij}\cdot\mu_i\left(\nabla\mathbf{u}_i + (\nabla\mathbf{u}_i)^T\right)\cdot\mathbf{e}_x \,\mathrm{d}\Gamma}_{d_{ij}^\mu}. \quad (19)$$

Fig. 16 shows the relative part of the viscous (d_f^μ) and pressure terms (d_f^p) in the fluid-fluid drag. The viscous term is negligible compared to the pressure part for very thin gaps $h^* \leq 1/4$ and for every value of Ca, as previously shown. In contrast, the viscous drag dominates over the pressure drag for low Ca and very thick gaps. Both terms are important for high Ca and thick gaps/2D flow.

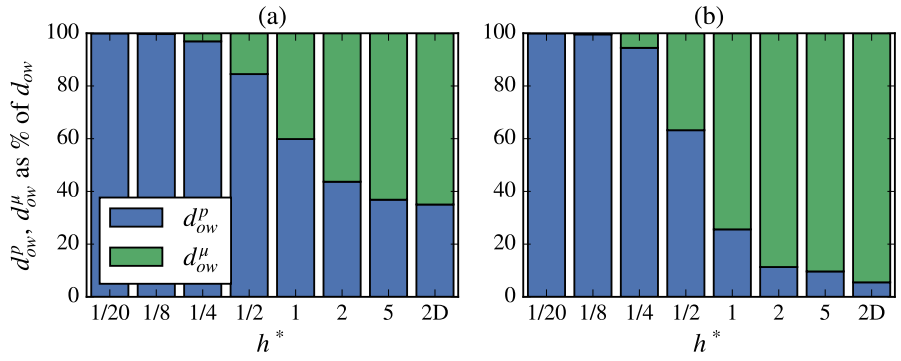

Figure 16: Part of viscous and pressure drag into the fluid-fluid drag force for different dimensionless gap thickness. (a) $Ca = 5 \times 10^{-1}$ and (b) $Ca = 2.5 \times 10^{-2}$. Here, $M = 1$, $f_f = 0.25$, and the results are obtained in UC4 at steady-state. The viscous drag is negligible compared to the pressure drag for thin gap $h^* \leq 0.25$.

5. Conclusions

The question of active or passive fluid-fluid interface (i.e. allows or not momentum exchange from one fluid to another) is of major concern for two-

phase flows in microfluidic devices, and by extension in porous media. This issue has been treated recently for remobilization of ganglia, for which the drag exerted by the surrounding flowing fluid is capital. Although not manifesting itself in such a visual way, fluid-fluid drag may also be important in the case of continuous film flow (i.e. the two fluids are flowing adjacently in the same channel), as the common interface is large. We addressed this question by numerical simulations in a modified Hele-Shaw cell, which allows calculating the contribution from the viscous shear, but also from the pressure contrary to the previous work, in the fluid-fluid drag.

We found that the fluid-fluid drag is not negligible, even for small gaps between the cell's plate (i.e. increasing solid-fluid friction). For an increasing gap, the fluid-fluid drag is more and more important to predict the pressure drop, especially for high capillary numbers. As an example, for $Ca = 0.5$, the fluid-fluid drag represents between 30% to 65% of the non-wetting fluid's pressure drop for a dimensionless gap increasing from 1/20 to 1. Also, we found that the pressure contribution may overcome the viscous shear contribution for smaller gaps.

The main limit of this work is the presence of the cylindrical solid obstacles between the cell's plates, also discussed in past similar works. The no-flow boundary condition induced a more complex flow field near the obstacle that is not well reproduced by the depth-averaged 2D flow equation. However, this issue is not strengthened by increasing the gap, which allows us to compare the results as we have done. These findings are important to predict and model two-phase flows in microfluidic devices when film-flow regimes are expected. They also add arguments in favor of taking into ac-

count the coupling between the two fluids in the large-scale flow equations used for highly permeable media, as film flow is a common regime in such porous media. Further work could investigate the dynamic film effects in the case of zero contact angle between the cell plates and the impact on the drag forces on them. However, this likely requires computationally intensive 3D flow calculations in order to accurately capture the films.

6. Acknowledgements

This work was supported by the French Geological Survey (BRGM) within the framework of the PSO MULTISCALEXPER project. The authors would like to thank the French Environment and Energy Management Agency (ADEME) and BRGM for providing the Ph.D. grant for Maxime Cochennec. We gratefully acknowledge the financial support provided to the PIVOTS project by the "Région Centre – Val de Loire" and the European Regional Development Fund.

References

Alamooti, A.H.M., Azizi, Q., Davarzani, H., 2020. Direct numerical simulation of trapped-phase recirculation at low capillary number. Advances in Water Resources 145, 103717.

Anderson, W.G., et al., 1987. Wettability literature survey part 5: the effects of wettability on relative permeability. Journal of Petroleum Technology 39, 1–453.

Attou, A., Boyer, C., Ferschneider, G., 1999. Modelling of the hydrodynamics of the cocurrent gas–liquid trickle flow through a

trickle-bed reactor. Chemical Engineering Science 54, 785 – 802. doi:https://doi.org/10.1016/S0009-2509(98)00285-1.

Auriault, J., Sanchez-Palencia, E., 1986. Remarques sur la loi de darcy pour les écoulements biphasiques en milieu poreux. Journal of Theoretical and Applied Mechanics, Numéro Spécial , p141–156.

Avraam, D.G., Payatakes, A.C., 1995. Generalized relative permeability coefficients during steady-state two-phase flow in porous media, and correlation with the flow mechanisms. Transport in Porous Media 20, 135–168. doi:10.1007/bf00616928.

Ayodele, O.R., 2006. Theoretical analysis of viscous coupling in two-phase flow through porous media. Transport in porous media 64, 171–184.

Ayub, M., Bentsen, R.G., 1999. Interfacial viscous coupling: a myth or reality? Journal of Petroleum Science and Engineering 23, 13–26.

Bacri, J.C., Chaouche, M., Salin, D., 1990. Modèle simple de perméabilités relatives croisées. Comptes rendus de l'Académie des sciences. Série 2, Mécanique, Physique, Chimie, Sciences de l'univers, Sciences de la Terre 311, 591–597.

Bashir, S., Rees, J.M., Zimmerman, W.B., 2014. Investigation of pressure profile evolution during confined microdroplet formation using a two-phase level set method. International journal of multiphase flow 60, 40–49.

Bensimon, D., 1986. Stability of viscous fingering. Physical Review A 33, 1302.

Bentsen, R.G., Manai, A.A., 1993. On the use of conventional cocurrent and countercurrent effective permeabilities to estimate the four generalized permeability coefficients which arise in coupled, two-phase flow. Transport in Porous Media 11, 243–262.

Bianchi Janetti, E., Riva, M., Guadagnini, A., 2017. Effects of pore-scale geometry and wettability on two-phase relative permeabilities within elementary cells. Water 9, 252.

Blunt, M.J., 2017. Multiphase flow in permeable media: A pore-scale perspective. Cambridge University Press.

Bourbiaux, B.J., Kalaydjian, F.J., et al., 1990. Experimental study of cocurrent and countercurrent flows in natural porous media. SPE Reservoir Engineering 5, 361–368.

Brooks, R., Corey, T., 1964. Hydrau uc properties of porous media. Hydrology Papers, Colorado State University 24, 37.

Chen, J., Sun, S., Wang, X., 2019. Homogenization of two-phase fluid flow in porous media via volume averaging. Journal of Computational and Applied Mathematics 353, 265–282.

Clavier, R., Chikhi, N., Fichot, F., Quintard, M., 2017. Modeling of inertial multi-phase flows through high permeability porous media: Friction closure laws. International Journal of Multiphase Flow 91, 243–261.

Cueto-Felgueroso, L., Juanes, R., 2014. A phase-field model of two-phase hele-shaw flow. Journal of fluid mechanics 758, 522.

Davit, Y., Quintard, M., 2018. One-phase and two-phase flow in highly permeable porous media. Heat Transfer Engineering , 1–19.

Dullien, F.A., 1992. Porous media: fluid transport and pore structure. 2 ed., Academic press.

Dullien, F.A.L., Dong, M., 1996. Experimental determination of the flow transport coefficients in the coupled equations of two-phase flow in porous media. Transport in Porous Media 25, 97–120. doi:10.1007/bf00141264.

Ehrlich, R., 1993. Viscous coupling in two-phase flow in porous media and its effect on relative permeabilities. Transport in Porous Media 11, 201–218.

Fetter, C.W., Boving, T., Kreamer, D., 2017. Contaminant hydrogeology. Waveland Press.

Gray, W.G., Miller, C.T., 2005. Thermodynamically constrained averaging theory approach for modeling flow and transport phenomena in porous medium systems: 1. motivation and overview. Advances in Water Resources 28, 161–180.

Gray, W.G., Miller, C.T., 2014. Introduction to the thermodynamically constrained averaging theory for porous medium systems. Springer.

Guyon, E., Hulin, J.P., Petit, L., 1994. Hydrodynamique physique. interéditions.

Heshmati, M., Piri, M., 2018. Interfacial boundary conditions and residual trapping: A pore-scale investigation of the effects of wetting phase flow

rate and viscosity using micro-particle image velocimetry. Fuel 224, 560 – 578. doi:https://doi.org/10.1016/j.fuel.2018.03.010.

Homsy, G.M., 1987. Viscous fingering in porous media. Annual review of fluid mechanics 19, 271–311.

Horgue, P., Augier, F., Duru, P., Prat, M., Quintard, M., 2013. Experimental and numerical study of two-phase flows in arrays of cylinders. Chemical Engineering Science 102, 335–345.

Jackson, S., Power, H., Giddings, D., Stevens, D., 2017. The stability of immiscible viscous fingering in hele-shaw cells with spatially varying permeability. Computer Methods in Applied Mechanics and Engineering 320, 606–632.

Karadimitriou, N., Hassanizadeh, S., 2012. A review of micromodels and their use in two-phase flow studies. Vadose Zone Journal 11.

Kopf-Sill, A.R., Homsy, G., 1988. Bubble motion in a hele–shaw cell. The Physics of fluids 31, 18–26.

Lasseux, D., Quintard, M., Whitaker, S., 1996. Determination of permeability tensors for two-phase flow in homogeneous porous media: theory. Transport in Porous Media 24, 107–137.

Lenormand, R., Touboul, E., Zarcone, C., 1988. Numerical models and experiments on immiscible displacements in porous media. Journal of fluid mechanics 189, 165–187.

Li, H., Pan, C., Miller, C.T., 2005. Pore-scale investigation of viscous coupling effects for two-phase flow in porous media. Physical Review E 72. doi:10.1103/physreve.72.026705.

Liu, J., Ju, Y., Zhang, Y., Gong, W., 2019. preferential paths of air-water two-phase flow in porous structures with special consideration of channel thickness effects. Scientific reports 9, 1–13.

Marle, C.M., 1982. On macroscopic equations governing multiphase flow with diffusion and chemical reactions in porous media. International Journal of Engineering Science 20, 643 – 662. doi:https://doi.org/10.1016/0020-7225(82)90118-5.

Maruvada, S., Park, C.W., 1996. Retarded motion of bubbles in hele–shaw cells. Physics of fluids 8, 3229–3233.

Maxworthy, T., 1986. Bubble formation, motion and interaction in a hele-shaw cell. Journal of Fluid Mechanics 173, 95–114.

Meiburg, E., Homsy, G., 1988. Nonlinear unstable viscous fingers in hele–shaw flows. ii. numerical simulation. The Physics of fluids 31, 429–439.

Morrow, N.R., Cram, P.J., McCaffery, F., et al., 1973. Displacement studies in dolomite with wettability control by octanoic acid. Society of Petroleum Engineers Journal 13, 221–232.

Muskat, M., 1938. The flow of homogeneous fluids through porous media. Soil Science 46, 169.

Nagel, M., Gallaire, F., 2015. Boundary elements method for microfluidic two-phase flows in shallow channels. Computers & Fluids 107, 272–284.

Olsson, E., Kreiss, G., 2005. A conservative level set method for two phase flow. Journal of Computational Physics 210, 225 – 246. doi:https://doi.org/10.1016/j.jcp.2005.04.007.

Olsson, E., Kreiss, G., Zahedi, S., 2007. A conservative level set method for two phase flow ii. Journal of Computational Physics 225, 785 – 807. doi:https://doi.org/10.1016/j.jcp.2006.12.027.

Park, C.W., Homsy, G., 1984. Two-phase displacement in hele shaw cells: theory. Journal of Fluid Mechanics 139, 291–308.

Rakotomalala, N., Salin, D., Yortsos, Y.C., 1995. Viscous coupling in a model porous medium geometry: Effect of fluid contact area. Applied scientific research 55, 155–169.

Ramakrishnan, T.S., Goode, P.A., 2015. Measurement of off-diagonal transport coefficients in two-phase flow in porous media. Journal of colloid and interface science 449, 392–398.

Roman, S., Soulaine, C., Kovscek., A.R., 2019. Pore-scale visualization and characterization of viscous dissipation in porous media. Journal of Colloid and Interface Science doi:https://doi.org/10.1016/j.jcis.2019.09.072.

Rose, W., 1988. Measuring transport coefficients necessary for the description of coupled two-phase flow of immiscible fluids in porous media. Transport in Porous Media 3, 163–171. URL: https://doi.org/10.1007/BF00820343, doi:10.1007/BF00820343.

Rothman, D.H., 1990. Macroscopic laws for immiscible two-phase flow in porous media: Results from numerical experiments. Journal of Geophysical Research 95, 8663. doi:10.1029/jb095ib06p08663.

Saffman, P.G., Taylor, G.I., 1958. The penetration of a fluid into a porous medium or hele-shaw cell containing a more viscous liquid. Proceedings of the Royal Society of London. Series A. Mathematical and Physical Sciences 245, 312–329.

de Santos, J.M., Melli, T.R., Scriven, L.E., 1991. Mechanics of gas-liquid flow in packed-bed contactors. Annual Review of Fluid Mechanics 23, 233–260. doi:10.1146/annurev.fl.23.010191.001313.

Schmidt, W., 2007. Interfacial drag of two-phase flow in porous media. International Journal of Multiphase Flow 33, 638 – 657. URL: http://www.sciencedirect.com/science/article/pii/S0301932206001662, doi:https://doi.org/10.1016/j.ijmultiphaseflow.2006.09.006.

Scott, P., Rose, W., et al., 1953. An explanation of the yuster effect. Journal of Petroleum Technology 5, 19–20.

Stokes, J., Weitz, D., Gollub, J.P., Dougherty, A., Robbins, M., Chaikin, P., Lindsay, H., 1986. Interfacial stability of immiscible displacement in a porous medium. Physical review letters 57, 1718.

Van Genuchten, M.T., 1980. A closed-form equation for predicting the hydraulic conductivity of unsaturated soils 1. Soil science society of America journal 44, 892–898.

Whitaker, S., 1986. Flow in porous media II: The governing equations for immiscible, two-phase flow. Transport in porous media 1, 105–125.

Whitaker, S., 1999. The Method of Volume Averaging. Springer, Dordrecht.

Wyckoff, R.D., Botset, H.G., 1936. The flow of gas-liquid mixtures through unconsolidated sands. Physics 7, 325–345.

Yiotis, A.G., Psihogios, J., Kainourgiakis, M.E., Papaioannou, A., Stubos, A.K., 2007. A lattice boltzmann study of viscous coupling effects in immiscible two-phase flow in porous media. Colloids and Surfaces A: Physicochemical and Engineering Aspects 300, 35 – 49. doi:https://doi.org/10.1016/j.colsurfa.2006.12.045.

Yuster, S., et al., 1951. Theoretical considerations of multiphase flow in idealized capillary systems, in: Proceedings of the Third World Petroleum Congress, E. Brill The Hague. pp. 437–445.

Zarcone, C., Lenormand, R., 1994. Détermination expérimentale du couplage visqueux dans les écoulements diphasiques en milieu poreux. Comptes rendus de l'Académie des sciences. Série II, Mécanique, physique, chimie, astronomie 318, 1429–1435.

Zhang, C., Oostrom, M., Wietsma, T.W., Grate, J.W., Warner, M.G., 2011. Influence of viscous and capillary forces on immiscible fluid displacement: Pore-scale experimental study in a water-wet micromodel demonstrating viscous and capillary fingering. Energy & Fuels 25, 3493–3505.

Appendix A. Comparison between 3D and depth-averaged 2D one-phase flows

In this appendix section we compare 3D and depth-averaged 2D one-phase flows to illustrate the impact of the gap thickness. The geometry is the same as used previously (3D model is obtained by an extrusion). First, Fig. A.17 shows the velocity profile (x-component) along a line from the tip of the cylindrical obstacle to the center of the pore (along y-axis) as a function of the dimensionless gap thickness. We observe a difference between the 2D and 3D results, even for a small gap thickness. This is due to the cylindrical solid obstacles that which locally disturbs the velocity field and which can only be obtained by 3D models. We note that this effect is not amplified by going outside the theoretical validity domain ($h/L \ll 1$), and that the depth-averaged 2D model is still effective.

This has an impact on the calculation of the drag on the cylindrical solid obstacle. As shown in Fig. A.18, the drag per unit of surface is well reproduced for gaps as large as $h/L = 2$.

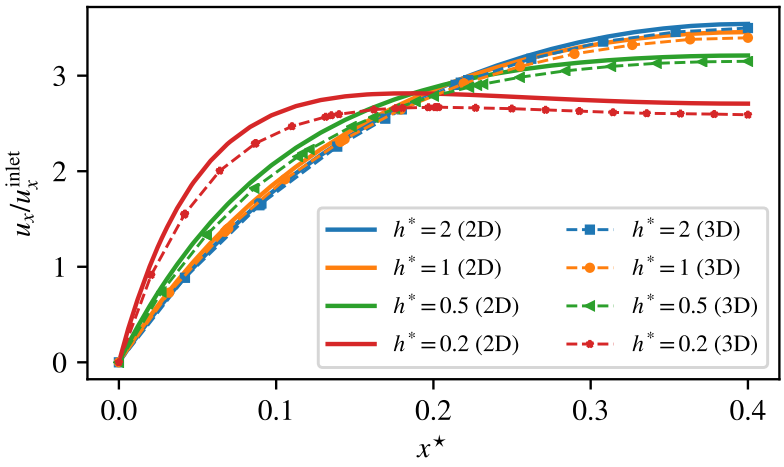

Figure A.17: Normalized velocity (x-component) profile along the line that goes from the tip of the obstacle to the center of the cell (along the y axis), for 2D depth-integrated and integrated 3D flow as a function of the dimensionless gap thickness.

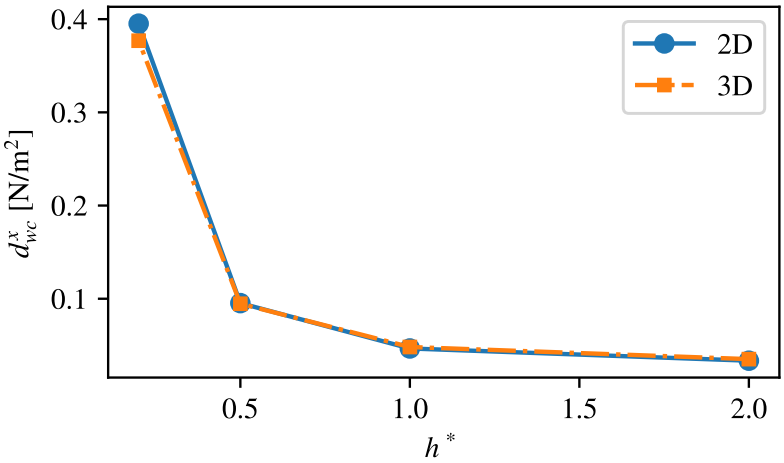

Figure A.18: Drag (x-component) per unit of surface, for 2D depth-integrated and 3D flows as a function of the dimensionless gap thickness.